Seabed Backscattered Signal Peak Shift and Broadening Induced by Multiple Scattering in Bathymetric Lidar

Mingjia Shangguan, Zhuoyang Liao, Yirui Guo, and Zhongping Lee, *Senior Member, IEEE*

***Abstract*— Bathymetric lidar, with its deep penetration, continuous day-and-night operation, and high accuracy, is an important tool for remotely sensing bottom depths. However, the strong forward scattering of the laser beam during transmission in water introduces substantial multiple scattering components into the lidar signal reflected by sea bottom, leading to a peak shift and signal broadening. The peak shift leads to an overestimation of the bottom depth, while the signal broadening makes peak extraction more challenging. To quantitatively study this impact, a semianalytic Monte Carlo (MC) simulation is applied to model seabed reflected signals. By statistically analyzing the peak position bias (termed as Bias) and full-width at half-maximum (termed as FWHM) of the seabed lidar reflected signals across four platforms—spaceborne, airborne, shipborne, and underwater—empirical models are established to relate Bias and FWHM to scattering efficient (b), bottom depth (z_m), and lidar receiver footprint (r_s). Here, r_s represents the radius of the footprint of the lidar receiver on the water surface. Furthermore, the effects of different scattering phase functions and the absorption coefficient are analyzed. This study shows that the Bias and FWHM are influenced by b, z_m, and r_s. For lidar systems with an r_s of dozens of meters, measuring deeper depths in water with higher b can result in a bottom depth overestimation of nearly 4% and an FWHM broadening exceeding 28 ns solely due to multiple scattering effects. This article provides a theoretical basis for correcting and evaluating bathymetric lidar data, thereby improving the accuracy and applicability of bathymetric lidar results.**

***Index Terms*— Bathymetry, lidar, Monte Carlo (MC), multiple scattering.**

I. Introduction

BATHYMETRIC data play an important role in supporting various marine operations, such as maritime navigation [1], port construction [2], the laying of subsea pipelines and cables [3], [4], planning offshore activities [5], and other oceanographic research initiatives [6], [7]. Currently, sonar technology is widely employed in depth measurement, utilizing both single-beam and multibeam techniques [8], [9]. However, sonar systems cannot operate across the air–sea interface and can only be deployed underwater, while multipath interference poses significant challenges for effective detection in shallow water environments [10], [11].

Optical remote sensing technologies enable bathymetric measurements across the air–sea interface with high spatial resolution and extensive coverage [12]. One such technique is ocean color remote sensing, which estimates bottom depth by measuring remote sensing reflectance [12], [13], [14], [15], [16]. However, ocean color remote sensing is constrained by light conditions and cloud cover, making observations impossible in conditions such as the absence of sunlight or under low sun angles [17], [18].

Fortunately, as an active optical remote sensing technology, bathymetric lidar can provide observations both day and night, along with high-precision and high-depth resolution measurements. This capability makes it an important complement to ocean color remote sensing. Moreover, by emitting laser pulses and analyzing the time it takes for the return signal from the water surface and bottom, lidar provides time information on both the water surface [19] and bottom, achieving a penetration depth three times greater than that of passive ocean color remote sensing [20].

To extend the observational coverage of lidar, different platforms for lidar systems have been developed and extensively applied, including spaceborne, airborne, shipborne, and underwater platforms [21]. Airborne lidar is well-suited for applications requiring high precision and broad coverage, providing exceptional accuracy and extensive measurement range. Typical systems include the airborne oceanographic lidar (AOL) developed by NASA, the laser airborne depth sounder (LADS) used by the Royal Australian Navy, and the scanning hydrographic operational airborne laser survey (SHOALS) employed by the U.S. Army Corps of Engineers, among others [22]. To support applications on smaller platforms, such as drones, researchers have developed and commercialized compact airborne depth measurement lidar systems. Examples include the RIEGL VQ-840-G [20], ASTRALiTe edge[1] [23],

Received 6 September 2024; revised 21 December 2024; accepted 29 January 2025. Date of publication 7 February 2025; date of current version 18 February 2025. This work was supported in part by the National Natural Science Foundation of China under Grant 42476184, in part by the National Key Research and Development Program of China under Grant 2022YFB3901704, in part by the Fundamental Research Funds for the Central Universities under Grant 20720200107, in part by Xiamen Natural Science Foundation General Project under Grant 2024FCX012503010164, and in part by the Joint Funds of the National Natural Science Foundation of China under Grant U2106210. *(Corresponding author: Mingjia Shangguan.)*

The authors are with the State Key Laboratory of Marine Environmental Science, College of Ocean and Earth Sciences, Xiamen University, Xiamen 361102, China (e-mail: mingjia@xmu.edu.cn; lzhyang@stu.xmu.edu.cn; gyirui@stu.xmu.edu.cn; zhongping.lee@umb.edu).

Digital Object Identifier 10.1109/TGRS.2025.3538989

[1]Trademarked.

and Fugro RAMMS [24]. While airborne lidar systems offer exceptional accuracy and broad coverage for ground-based measurements, spaceborne lidar systems are crucial for global-scale observations and long-term monitoring. ICESat-2, for example, is equipped with the advanced single-photon geophysical lidar altimeter system (ATLAS). Although ATLAS is not specifically designed for seabed depth measurement, it has been validated to detect depths of approximately 40 m, with root-mean-square error (RMSE) values ranging from 0.26 to 0.61 m [25], [26]. Moreover, to avoid interference from the air–sea interface, miniaturized single-photon lidar systems have been proposed and demonstrated, and are suitable for application on underwater autonomous underwater vehicles (AUVs) and remotely operated vehicles (ROVs) [27].

However, when lidar penetrates the air–sea interface for depth measurements, corrections are required to account for errors caused by water surface fluctuations and refraction at the air–sea interface [25], [28], [29], [30], [31], [32], [33], [34]. Additionally, due to the strong forward scattering of laser light during transmission in the water, some photons deviate from their original path and reach the seabed, causing the photon transmission path to be longer than the bottom depth, which leads to an overestimation of the measured depth [35]. Studies have shown that there is a relationship between the bathymetric error and the backscattering coefficient of the ICESat-2 satellite [36]. Moreover, although a larger field of view (FOV) on lidar systems increases the received signal level to achieve a deeper depth, it simultaneously introduces bathymetric errors due to multiple scattering of photons in the water column. Furthermore, for full-waveform bathymetric lidar, previous studies have indicated that the waveform decomposition method can partially mitigate the forward-scattering bias in water [37], [38]. However, bathymetric errors caused by multiple scattering are influenced by a combination of the optical properties of the water, bottom depth, and the hardware parameters of the lidar system. This study comprehensively investigates and quantitatively analyzes the impact of these three factors on the peak position bias (termed as Bias) and full-width at half-maximum (FWHM) of seabed lidar reflected signals across four platforms.

In fact, the reflected waveform from the bottom $S(t, z)$ measured by a bathymetric lidar is the result of the convolution of the lidar's response function $L(t)$, the water body response function $R(t)$, and the bottom topography influence function $d(t, z)$, which can be expressed as [36]

$$S(t, z) = L(t) \otimes R(t) \otimes d(t, z) \tag{1}$$

where $\otimes$ represents a convolution operation. $L(t)$ represents the lidar's response function, which includes the effects of pulsewidth, the response speed of the detector, and the sampling rate of the acquisition card. $R(t)$ is the water body's response to the laser pulse, primarily caused by multiple scattering of the laser as it propagates through the water. The multiple scattering effects not only shift the peak position of the seabed's reflected signal, but also affect the temporal width of the signal [39]. $d(t, z)$ represents the influence of the bottom topography on the reflected waveform. Here, t is the time variable, representing the delay of the reflected signal, while z represents the depth or height of the bottom, reflecting the topographic undulations of the seabed. The unevenness of the bottom leads to different reflection times at different locations, which, in turn, affects the time delay and waveform shape of the reflected signal. To simplify the analysis, this study considers only the effect of multiple scattering on the bottom-reflected signal. After analyzing the effects of multiple scattering, thereby establishing the expression for $R(t)$, the influence of $L(t)$ and $d(t, z)$ on the seabed reflected signal can be analyzed according to different lidar parameters, including platform and hardware parameters, as well as the seabed structure, using (1).

The structure of this article is as follows. First, semi-analytical Monte Carlo (MC) simulations are conducted to record the seabed reflected signals for four types of lidar platforms. Subsequently, analytical expressions are established for the relationship between the peak bias and broadening of seabed reflected signal with the inherent optical properties (IOPs) of the water, bottom depth, and r_s, which represents the radius of the footprint of the lidar receiver on the water surface, and these are discussed separately for four platforms. Moreover, the impact of various scattering phase functions (SPFs) and the absorption coefficient on bathymetric lidar is further analyzed. Finally, conclusions are presented.

II. MC Simulation

A. Semianalytic MC Simulation

In ocean lidar applications, MC has been experimentally validated for simulating ocean signals [40], [41], [42], [43], and MC for simulating elastic scattering [44], [45], [46], inelastic scattering [40], and polarization scattering [47], [48] in ocean lidar has also been developed. Here, the process of MC simulation for simultaneously recording the seabed reflected signal is briefly introduced. The semianalytical MC method, which has been validated to obtain consistent results with the conventional MC method that considers the laser double-path, while significantly enhancing simulation efficiency, is employed to simulate the reflected signals from the seabed [49]. The simulation flowchart is shown in Fig. 1.

During the simulation, a coordinate system is first established, with the geometric center of the receiver's FOV on the water surface as the origin and the z-axis oriented downward. Next, the state of the photons is initialized: the photon position (x, y, z) is set to $(x_0, y_0, 0)$, where x_0 and y_0 are the random values that match the distribution of the incident light spot on the water surface; the photon direction (u_x, u_y, u_z) is initialized to (0, 0, 1); the photon weight W_0 is set to 1, and the threshold for photon weight W_T is set to $1 \cdot 10^{-10}$. Then, the step length (s) and the updated photon weight (W_{n+1}) are calculated based on the IOPs of water [50]. When the photon weight falls below the threshold W_T, the photon is considered extinct. Afterward, the new direction vector (u'_x, u'_y, u'_z) is calculated using the scattering angle θ and the azimuthal angle φ [50]. Once the photon's step length and movement direction are determined, the new position (x', y', z') is computed. Finally, it is checked whether the photon is within the receiver's FOV: if it is, the data are

TABLE I
KEY PARAMETERS OF LIDAR SYSTEMS

Parameter	ICESat-2	Airborne 3 km	Airborne 0.35 km	Shipborne	Underwater
Wavelength of laser	532 nm	532 nm	532 nm	532 nm	532 nm
Beam spot radius of the emitted laser	2.5 mm	25 mm	3.25 mm	10 mm	2 mm
Laser divergence angle	0.035 mrad	2.4 mrad	0.25 mrad	1 mrad	0.5 mrad
Laser beam spot radius on water surface	<8.7 m	3.6 m	0.4375 m	0.005 m	None
Aperture of the telescope	800 mm	200 mm	200 mm	50.8 mm	6 mm
FOV of the receiver	0.0884 mrad	25 mrad	6 mrad	200 mrad	3.8 mrad
Receiver footprint	45 m	75.2 m	2.3 m	2.06 m	None
Vertical height	500000 m	3000 m	350 m	10 m	None
Tilt angle	2.0002°	3°	15°	60°	None
References	[61]	[62]	[63, 64]	[65]	[27]

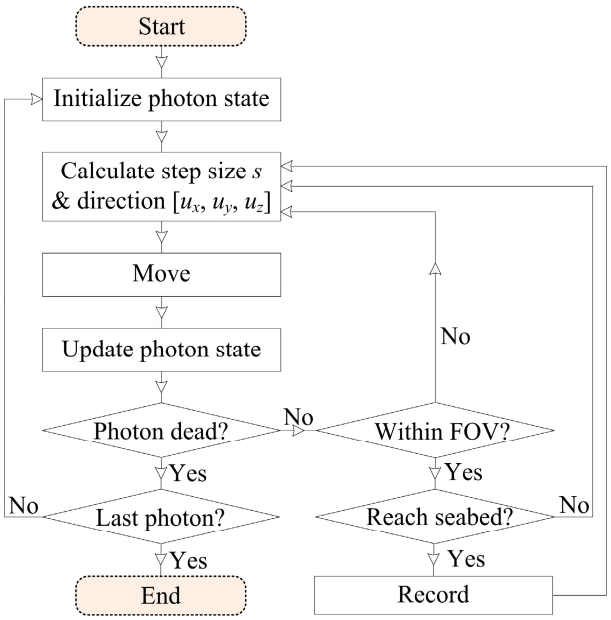

Fig. 1. Flowchart of MC simulation.

recorded; if not, the photon tracking ceases. For vertically incident laser light, a photon is considered within the receiver's FOV if its position (x, y, z) satisfies the following conditions:

$$x^2 + y^2 \le \left[z \cdot \tan(\mathrm{FOV}_1/2) + r_s\right]^2 \tag{2}$$

where FOV_1 is the FOV after refraction at the water surface, and r_s is the radius of the receiver footprint on the water surface. FOV_1 and r_s can be expressed based on Snell's refraction law and geometric relationships. For laser incident at a specific tilt angle (as shown in Table I), the geometry of the receiving FOV changes accordingly [51].

The process simulates photon propagation within the water column, including scenarios where photons reach the seabed, are reflected, and are subsequently detected by the lidar receiver, with z_{mg} representing the real seabed depth. When the photon's depth prior to movement, z_{i-1}, satisfies $z_{i-1} < z_{mg}$, and the depth after movement, z_i, satisfies $z_i \ge z_{mg}$, the photon is considered to have reached the seabed, prompting an update to the photon's position and movement step length

$$\begin{cases} s' = \left|\left(z_{mg} - z_{i-1}\right)/(z_i - z_{i-1})\right| \cdot s \\ x' = x + u'_x s' \\ y' = y + u'_y s' \\ z' = z + u'_z s' \end{cases} \tag{3}$$

where s' represents the step length of the photon's movement from the previous position to the seabed; (x', y', z') represents the new position and (x, y, z) represents the photon position before movement. Subsequently, the photon undergoes reflection at the seabed. In this process, the seabed is treated as a Lambertian reflector, and the photon's position, direction, and weight are updated according to the law of reflection [52].

Since bathymetric lidar records signals based on the return time of photons, in the MC simulation, signals are recorded based on the distance traveled by photons. Fig. 2(a)–(c) illustrates the photon paths under the same seabed depth with different IOPs of the water. Path I represents the movement of photons in water with a low scattering coefficient (b). Due to fewer multiple scatterings and larger step length in this type of water, the actual distance traveled by photons deviates minimally from the bottom depth, resulting in the seabed signal peak position being very close to the actual bottom depth, with a narrower FWHM of the seabed signal. Path III represents the movement of photons in water with relatively high b values. The higher number of multiple scatterings and shorter step length in this type of water leads to a greater deviation of the seabed signal peak position from the bottom depth and causes the FWHM of the seabed signal to broaden. Path II represents the photon path when optical properties are intermediate between the two aforementioned cases, with the seabed signal peak shift and broadening falling between these two scenarios. To quantitatively analyze the peak deviation and broadening of the seabed signal caused by multiple scatterings, Section III will investigate the impact of different IOPs, r_s, and seabed depths on the seabed signal peak deviation and broadening under four typical platforms.

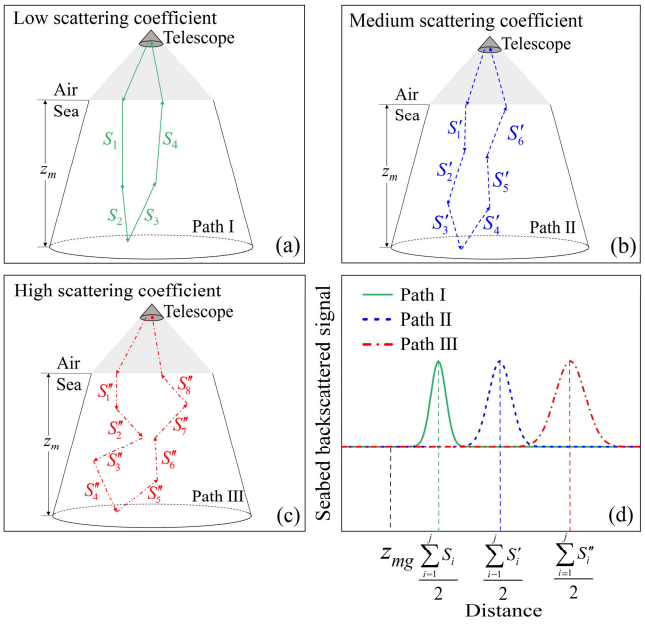

Fig. 2. Diagram of the impact of multiple scattering on seabed reflected signals. Schematic of photon paths in (a) low scattering coefficient (b). (b) Medium b. (c) High b. (d) Corresponding diagram of lidar measured seabed reflected signals, where j indicates the number of multiple scattering events for photons.

B. Bio-Optical Models of Water

First, the bio-optical model applied in the simulation is introduced. As mentioned above, the step length of photon movement is governed by the beam attenuation coefficient (c); when the incident wavelength of the laser is 532 nm, c can be expressed as

$$c(532, \mathrm{Chl}) = a(532, \mathrm{Chl}) + b(532, \mathrm{Chl}) \tag{4}$$

where Chl represents the chlorophyll-a concentration, and $a(532, \mathrm{Chl})$ is the absorption coefficient at 532 nm, which, for "Case-1" waters, can be expressed as [53]

$$a(532, \mathrm{Chl}) = a_w(532) + 0.06A(532) \cdot \mathrm{Chl}^{0.65} + a_y(532, \mathrm{Chl}) \tag{5}$$

where $a_w(532)$ is the absorption coefficient of pure seawater at 532 nm, with a value of 0.045 m^{-1} [54]; $A(532)$ represents a ratio of the absorption coefficient of phytoplankton at 532 nm versus that at 440 nm, with a value taken as 0.453 [55]; and $a_y(532, \mathrm{Chl})$ is the absorption coefficient for yellow substances at 532 nm, which can be expressed as [53]

$$\begin{cases} a_y(532, \mathrm{Chl}) = a_y(440, \mathrm{Chl}) \exp[-0.014(532 - 440)] \\ a_y(440, \mathrm{Chl}) = 0.2\left[a_w(440) + 0.06 \cdot \mathrm{Chl}^{0.65}\right] \end{cases} \tag{6}$$

where $a_w(440)$ is the absorption coefficient of pure seawater at 440 nm, with a value of 0.0044 m^{-1} [54]. In (4), the scattering coefficient $b(532, \mathrm{Chl})$ can be expressed as

$$b(532, \mathrm{Chl}) = b_w(532) + b_p(532, \mathrm{Chl}) \tag{7}$$

where $b_w(532)$ is the scattering coefficient of pure (sea)water at 532 nm, with a value of 2.232×10^{-3} m^{-1} [56], and for seawater, a salinity correction is needed [57]. $b_p(532, \mathrm{Chl})$ is the scattering coefficient of particles [58], and the models $b_p(532, \mathrm{Chl})$ at 532 nm are detailed as follows:

$$b_p(532, \mathrm{Chl}) = 0.3 \cdot \mathrm{Chl}^{0.62}(550/532). \tag{8}$$

Additionally, the maximum detectable depth of the lidar can be assessed based on the diffuse attenuation coefficient (K_d) at 532 nm, calculated using the model [59]

$$K_d(532) = m_0 \cdot a(532) + m_1\{1 - m_2 \exp[-m_3 a(532)]\} b_b(532) \tag{9}$$

where $m_0 \approx 1 + 0.005\theta_s$, with m_1, m_2, and m_3 taking values of 4.18, 0.52, and 10.8 [59], respectively; the model for $a(532)$ is shown in (5) and (6); and $b_b(532)$ represents the backscattering coefficient, which can be calculated using $b(532)$ when the scattering phase function is defined. In this study, the widely used Petzold scattering phase function is adopted [60].

It should be noted that although the formulas presented above focus on the optical parameters of 532 nm, the overall function is also applicable to other wavelengths, except that many values should be replaced to corresponding to the relevant wavelength when applying the aforementioned bio-optical models. Additionally, for simplicity, b and K_d refer to the scattering coefficient and the diffuse attenuation coefficient at 532 nm, respectively, with the same notation used thereafter.

C. Lidar Parameters

To study the impact of multiple scattering on the Bias and FWHM of seabed reflected signals, this article selected five typical platforms. The key parameters of the lidar systems for each platform are listed in Table I. To balance the simulation efficiency and the signal-to-noise ratio (SNR) of the simulated profile, 10^8 photons are used for simulating each profile.

D. MC Results

Since the strong specular reflection signal from the air–sea interface primarily interferes with the surface signals, and to improve simulation efficiency while highlighting the influence of multiple scattering on the bottom-reflected signal, the effect of the air–sea interface is neglected in the simulation. Additionally, to verify the effectiveness of the optimized simulation program, a comparison is carried out between the seabed reflected signal that records the water column signal and the one that does not, as shown in Fig. 3.

In the simulation process, to improve efficiency, only the bottom reflected signals are recorded, while the backscattered signal from the water is not. From Fig. 3, using the Airborne-0.35-km platform as an example, it can be seen that under four different conditions of IOPs and z_{mg}, the seabed reflected signals, with and without recording coincident water column signal, validate the effectiveness of the optimized simulation program. Furthermore, Fig. 3 shows that the SNR of the seabed reflected signal without recording the water column signal is significantly improved. Compared to the signal that records the water column backscatter, the simulation code that only models the seabed reflected signals runs about five times faster, further validating the increased efficiency of the optimized simulation software.

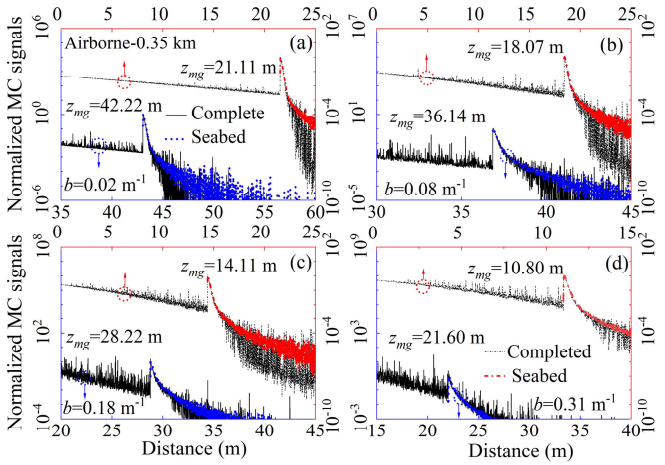

Fig. 3. Comparison of simulated seabed reflected signals with (black lines) and without (red and blue lines) recording the water column signal under varying conditions on the Airborne-0.35-km platform. (a) $b = 0.02$ m^{-1}, $z_{mg} = 1/K_d = 21.11$ m, and $z_{mg} = 2/K_d = 42.22$ m. (b) $b = 0.08$ m^{-1}, $z_{mg} = 1/K_d = 18.07$ m, and $z_{mg} = 2/K_d = 36.14$ m. (c) $b = 0.18$ m^{-1}, $z_{mg} = 1/K_d = 14.11$ m, and $z_{mg} = 2/K_d = 28.22$ m. (d) $b = 0.31$ m^{-1}, $z_{mg} = 1/K_d = 10.80$ m, and $z_{mg} = 2/K_d = 21.60$ m.

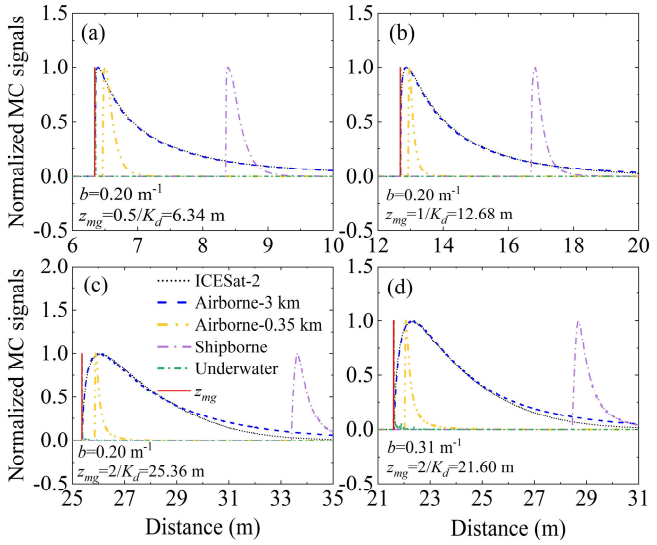

Fig. 4. Normalized simulated signals for five different platforms under varying conditions. (a) $b = 0.20$ m^{-1} and $z_{mg} = 0.5/K_d = 6.34$ m. (b) $z_{mg} = 1/K_d = 12.68$ m. (c) $z_{mg} = 2/K_d = 25.36$ m. (d) $b = 0.31$ m^{-1} and $z_{mg} = 2/K_d = 21.60$ m.

Using the parameters from Table I and the water bio-optical models in (4)–(9) with the Petzold scattering phase function, and with Chl set to 0.5 and 1.0 mg/m^3, the simulated seabed reflected signals with different seabed depths across various platforms are shown in Fig. 4. In the MC simulation, the sampling length, defined as the total distance over which photon interactions are tracked, is set to 100 m with a sampling interval of 0.01 m. To simplify this study, the simulation process assumes a homogeneous distribution of the water column.

From Fig. 4, it can be observed that, with the same b and z_{mg}, there are significant differences in the depth deviation and the broadening of seabed backscattered signals across different platforms. Note that the signal in Fig. 4 is the raw signal at the corresponding tilt angle and has not been angle-corrected. As a result, due to the large tilt angle of the shipborne lidar, the seabed reflected waveform is delayed in the time domain. Additionally, as the height of the platform above the water surface increases, the r_s becomes larger, and the differences become more pronounced. Furthermore, for the same platform and b value, Fig. 4(a)–(c) demonstrates that with increasing z_{mg}, both depth deviation and broadening increase. For the same platform and fixed z_{mg}, an increase in b results in greater depth deviation and broadening. Thus, from Fig. 4, it is evident that depth deviation and broadening are influenced not only by r_s but also by b and z_{mg}. This is because all three factors affect the proportion of multiple scattering signals in the reflected signal. For example, with ICESat-2, the distribution of multiple scattering signals under different b and z_{mg} values is shown in Fig. 5. Comparing Fig. 5(a) and (b), with the same z_{mg}, increasing b leads to a higher proportion of multiple scattering in the bottom-reflected signal. Comparing Fig. 5(a)–(d), it is observed that with the same b, increasing z_{mg} also leads to a higher proportion of multiple scattering.

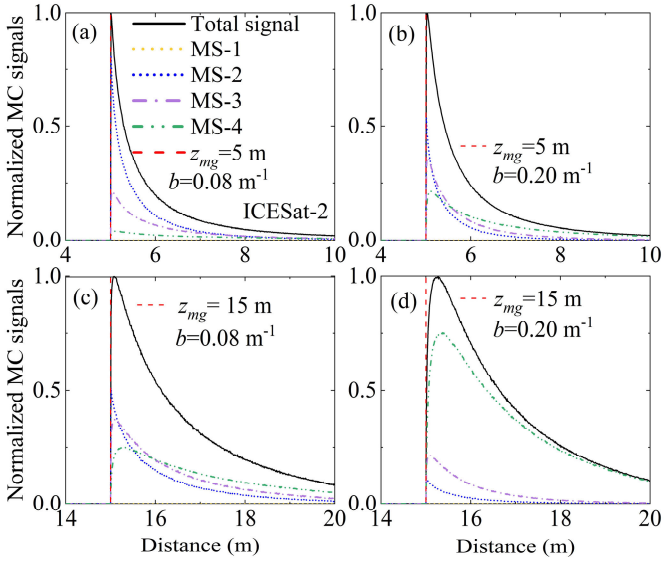

Fig. 5. (a) Simulated signals and multiple scattering for the ICESat-2 platform when $z_{mg} = 5$ m and $b = 0.08$ m^{-1}. (b) $b = 0.20$ m^{-1}. (c) $z_{mg} = 15$ m and $b = 0.08$ m^{-1}. (d) $z_{mg} = 15$ m and $b = 0.20$ m^{-1}. Here, MS-1 indicates the single scattering, MS-2 indicates the double scattering, MS-3 indicates the triple scattering, and MS-4 indicates the four or more scatterings.

Therefore, the next step will be to quantitatively analyze the relationships between b, z_{mg}, r_s, and depth deviation and signal broadening. Note that, for convenience in directly using the statistical model of Bias and FWHM, the subsequent statistics use the depth derived from the seabed reflected waveform (i.e., z_m) rather than the true depth (z_{mg}). The simulated seabed reflected signal is processed as follows: first, the "Findpeaks" function in MATLAB is used to identify the peak of the seabed reflected waveform. After correcting for the tilt angle, the difference between the extracted depth (z_m) and the true bottom depth (z_{mg}) is calculated, termed as Bias. Additionally, the FWHM of the seabed reflected waveform is calculated to quantify the broadening caused by multiple scatterings.

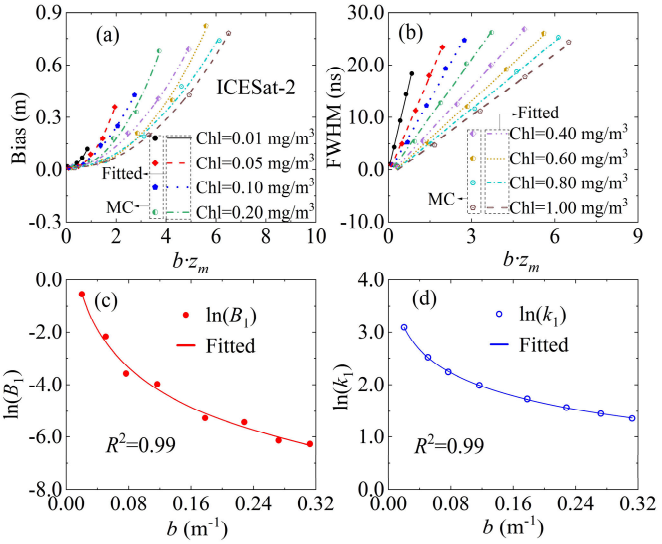

Fig. 6. For Chl from 0.01 to 1.00 mg/m^3, correspondingly, b ranging from 0.02 to 0.31 m^{-1}, and z_{mg} within $(0.1\sim2)/K_d$ on the ICESat-2 platform. (a) Relationship between peak position bias (Bias) and $b\cdot z_m$. (b) Relationship between FWHM and $b\cdot z_m$. Symbols represent MC simulation results; lines represent the fitting results from (10) and (11). (c) Relationship between fitting coefficients $\ln(B_1)$ in (a) with b. (d) Relationship between fitting slope $\ln(k_1)$ in (b) with b. Dots represent MC statistical results, and lines represent the fitting results of polynomial functions from (12) and (13).

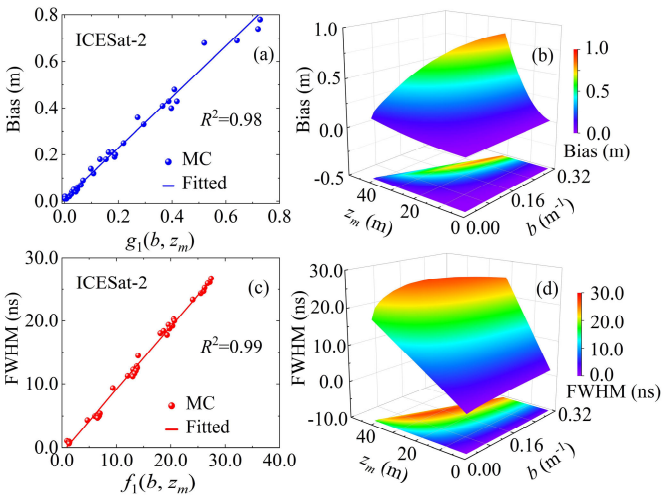

Fig. 7. For Chl from 0.01 to 1.00 mg/m^3, correspondingly, b ranging from 0.02 to 0.31 m^{-1}, and z_m within $(0.1\sim2)/K_d$ on the ICESat-2 platform. (a) Relationship between Bias and $g_1(b, z_m)$. (b) 3-D plot of Bias versus b and z_m based on (16). (c) Relationship between FWHM and $f_1(b, z_m)$. (d) 3-D plot of FWHM versus b and z_m based on (17).

III. Analysis of Bias and FWHM

A. ICESat-2

First, the MC simulation is applied to the ICESat-2 platform. The maximum bottom depth that can be measured by the ICESat-2 lidar is approximately $2/K_d$ [25]. In this study, as ~90% of the global surface ocean has Chl under 1 mg/m^3 [66] the range of Chl is set between 0.01 and 1.00 mg/m^3, subsequently the corresponding b values ranging from ~0.02 to 0.31 m^{-1}. Five different seabed depths are evaluated for each Chl value, corresponding to 0.1, 0.5, 1, 1.5, and 2 times of $1/K_d$. When $b\cdot z_m$ is used as an independent variable, the statistical results for the Bias and the FWHM of the seabed reflected signal are shown in Fig. 6(a) and (b), respectively. As shown in Fig. 6, the Bias of the seabed reflected signal for different depths under various b values follows a binomial relationship with $b\cdot z_m$, while the FWHM of reflected signal at different seabed depths follows a linear relationship with $b\cdot z_m$. Therefore, the following binomial function is used to fit the relationship between Bias and $b\cdot z_m$:

$$\text{Bias} = \text{constant}_1 + B_1\cdot(b\cdot z_m)^2 \tag{10}$$

where constant_1 is a constant, and B_1 is the binomial coefficient.

Similarly, the relationship between FWHM and $b\cdot z_m$ is fit using the following linear function:

$$\text{FWHM} = \text{constant}_2 + k_1\cdot(b\cdot z_m) \tag{11}$$

where constant_2 is the intercept and k_1 is the slope.

As shown in Fig. 6, both (10) and (11) can effectively fit the relationships between Bias and FWHM with $b\cdot z_m$, with the coefficient of determination (R^2) values exceeding 0.98. The differences in the curves shown in Fig. 6(a) and (b) are due to varying b values. The relationships between the fit B_1 and k_1 with b are shown in Fig. 6(c) and (d). From Fig. 6(c), as b increases, B_1 in (10) decreases exponentially. The relationships between b and $\ln(B_1)$ can be described by logarithmic functions, with R^2 values exceeding 0.99. Fig. 6(d) shows that as b increases, the slope k_1 decreases, and the relationship between b and $\ln(k_1)$ can be described by a logarithmic function, with an R^2 of 0.99. The functional relationships of b with B_1 and b with k_1 are as follows:

$$B_1 = e^{-4.97}/\left(b - 8.39\cdot10^{-4}\right)^{1.35} \tag{12}$$

$$k_1 = e^{0.63}/\left(b + 1.40\cdot10^{-4}\right)^{0.63}. \tag{13}$$

Subsequently, substituting (12) into (10) and (13) into (11) yields two new variables, represented as $g_1(b, z_m)$ and $f_1(b, z_m)$, respectively, which can be expressed as follows:

$$g_1(b, z_m) = \left[e^{-4.97}/\left(b - 8.39\cdot10^{-4}\right)^{1.35}\right]\cdot(b\cdot z_m)^2 \tag{14}$$

$$f_1(b, z_m) = \left[e^{0.63}/\left(b + 1.40\cdot10^{-4}\right)^{0.63}\right]\cdot(b\cdot z_m). \tag{15}$$

Fig. 7(a) shows the relationship between Bias and $g_1(b, z_m)$. A linear fit of this relationship yields the following result:

$$\text{Bias} = 1.072\cdot g_1(b, z_m) + 0.012. \tag{16}$$

Similarly, Fig. 7(c) shows the relationship between FWHM and $f_1(b, z_m)$, along with the results of a linear fit, which are as follows:

$$\text{FWHM} = 0.994\cdot f_1(b, z_m) - 0.786. \tag{17}$$

By substituting (14) into (16), the relationship between Bias and b as well as z_m can be obtained, as shown in Fig. 7(a). Similarly, substituting (15) into (17) provides the relationship between FWHM and b as well as z_m, as illustrated in Fig. 7(c). From Fig. 7(b) and (d), it can be observed that both Bias and FWHM increase with the increase in z_m and b. When both z_m and b are high, Bias can reach up to 0.8 m, and FWHM can reach up to 30 ns. This indicates that, under these conditions,

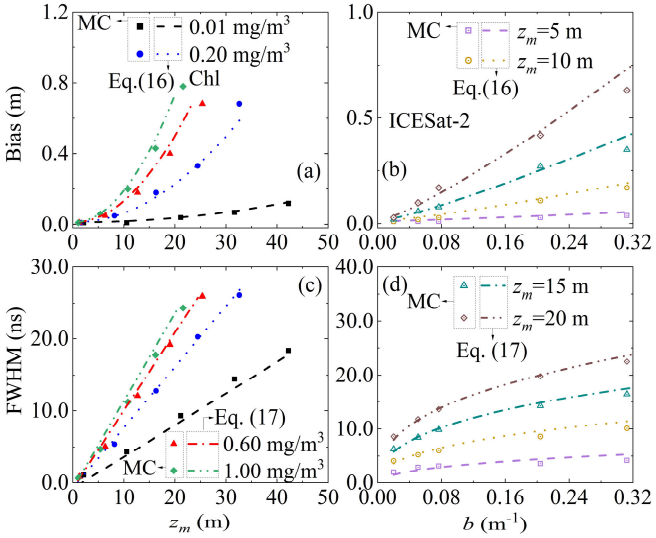

Fig. 8. (a) Bias versus z_m for different b values. (b) Bias versus b for different z_m values. (c) FWHM versus z_m for different b values. (d) FWHM versus b for different z_m values. Symbols represent MC simulation results, and lines represent the results computed from analytical expressions (16) and (17).

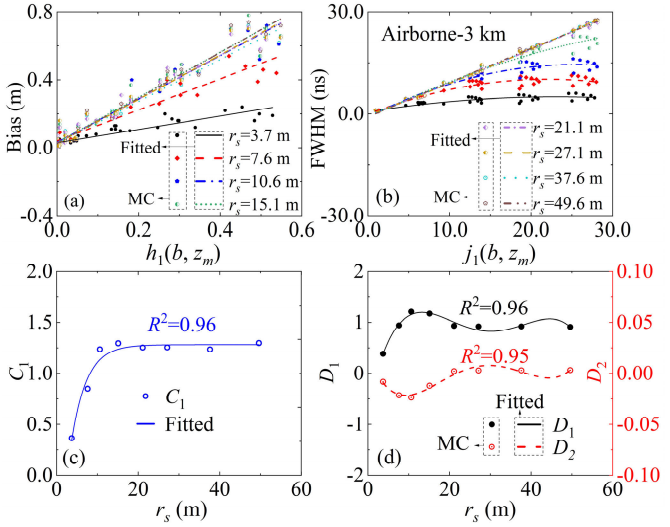

Fig. 9. For Chl ranging from 0.01 to 1.00 mg/m^3, b varies from 0.02 to 0.31 m^{-1}, and z_m ranges from $(0.1\sim2)/K_d$ on the Airborne-3-km platform. (a) Bias versus $h_1(b, z_m)$ and (b) FWHM versus $j_1(b, z_m)$ under different r_s conditions. The relationships between the fit parameters obtained from fitting the data in (a) and (b) using (18) and (19) with r_s. (c) C_1 versus r_s. (d) D_1 and D_2 versus r_s. Symbols represent the MC simulation results, while lines represent the fit results.

the effect of multiple scattering is significant, and it is essential to apply (16) for depth bias correction.

To clearly present the relationships between Bias and b as well as z_m, and between FWHM and b as well as z_m, Fig. 8(a) shows the relationship between Bias and z_m under different b values, while Fig. 8(c) shows the relationship between FWHM and z_m. The relationships between Bias and b, and between FWHM and b, are shown in Fig. 8(b) and (d), respectively. The symbols represent the MC simulation results, while the lines indicate results calculated using the analytical expressions in (16) and (17). Fig. 8 demonstrate that the results calculated using (16) and (17) are consistent with the MC simulation results, thereby validating the effectiveness of the empirical model.

B. Airborne-3 km

Compared to spaceborne lidar, airborne bathymetric lidar operates at a lower altitude above the water surface, thereby offering a wider range of selectable FOV. Therefore, this analysis considers not only the effects of b and z_m, but also the impact of r_s on the peak deviation and broadening of the seabed reflected signal. Following the previous analysis method, the effects of b and z_m on the seabed signal are first analyzed under an airborne platform with a height of 3 km above the water surface, followed by the inclusion of r_s to assess its impact on the seabed signal.

First, following the statistical method described for the ICESat-2 platform, the relationships between the Bias and FWHM of the seabed reflected signal and both b and z_m are fit separately. Then, the relationship between the fitting parameters and b is established to derive the normalized independent variables $h_1(b, z_m)$ for Bias and $j_1(b, z_m)$ for FWHM, as detailed in the following:

$$h_1(b, z_m) = 0.02 \cdot b \cdot z_m + [0.67 - 0.71 \ln(b - 0.02)] \cdot (b \cdot z_m)^2 \quad (18)$$

$$j_1(b, z_m) = \left[e^{0.44} \Big/ \left(b + 8.23 \cdot 10^{-3}\right)^{0.74}\right] \cdot (b \cdot z_m). \quad (19)$$

To study the performance of Bias and FWHM for the airborne lidar platform at different FOVs (i.e., different r_s values), MC simulations were conducted with the FOV adjusted from 2.4 to 33 mrad, while keeping other parameters constant. Subsequently, the relationships between Bias and $h_1(b, z_m)$ and between FWHM and $j_1(b, z_m)$ under different r_s conditions are calculated, as shown in Fig. 9(a) and (b), respectively. As can be seen from Fig. 9(a) and (b), the relationships between Bias and $h_1(b, z_m)$ and between FWHM and $j_1(b, z_m)$ can be fit using the following polynomials:

$$\text{Bias} = \text{constant}_3 + C_1 \cdot h_1(b, z_m) \quad (20)$$

$$\text{FWHM} = \text{constant}_4 + D_1 \cdot j_1(b, z_m) + D_2 \cdot \left[j_1(b, z_m)\right]^2 \quad (21)$$

where constant_3 and constant_4 are the constants, and C_1, D_1, and D_2 are the fit polynomial coefficients. Subsequently, the relationships between C_1, D_1, D_2, and r_s are analyzed and fit using power functions and polynomials, respectively. The resulting fit expressions are given as follows:

$$C_1 = 1.28 - 2.50 \cdot 0.77^{r_s} \quad (22)$$

$$\begin{cases} D_1 = -0.65 + 0.36 r_s - 0.02 r_s^2 + 5.90 \cdot 10^{-4} r_s^3 \\ \qquad - 5.03 \cdot 10^{-6} r_s^4 \\ D_2 = 0.018 - 0.01 r_s + 7.87 \cdot 10^{-4} r_s^2 \\ \qquad - 2.32 \cdot 10^{-5} r_s^3 + 2.08 \cdot 10^{-7} r_s^4. \end{cases} \quad (23)$$

Next, by substituting (22) into (20) and (23) into (21), two new normalized independent variables that take r_s into account are obtained, represented as $g_2(b, z_m, r_s)$ for Bias and

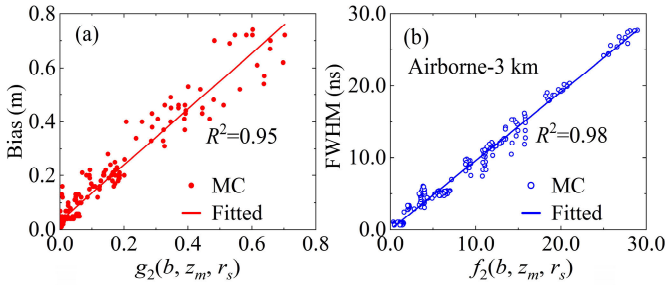

Fig. 10. For Chl ranging from 0.01 to 1.00 mg/m^3, b varies from 0.02 to 0.31 m^{-1}, and z_m ranges from (0.1∼2)/K_d on the Airborne-3-km platform. (a) Bias versus $g_2(b, z_m, r_s)$ and (b) FWHM versus $f_2(b, z_m, r_s)$. Symbols represent the MC simulation results, while lines represent the fit results.

$f_2(b, z_m, r_s)$ for FWHM, respectively,

$$\begin{cases} g_2(b, z_m, r_s) = C_1 \cdot h_1(b, z_m) \\ f_2(b, z_m, r_s) = D_1 \cdot j_1(b, z_m) + D_2 \cdot \left[j_1(b, z_m)\right]^2. \end{cases} \tag{24}$$

The relationship between Bias and $g_2(b, z_m, r_s)$ is shown by the symbols in Fig. 10(a). By performing a linear fit, a statistical expression for Bias in terms of b, z_m, and r_s is ultimately established, which can be expressed as

$$\text{Bias} = 1.036 \cdot g_2(b, z_m, r_s) + 0.032. \tag{25}$$

Similarly, the relationship between FWHM and $f_2(b, z_m, r_s)$ is shown by the symbols in Fig. 10(b). By performing a linear fit on the relationship between FWHM and $f_2(b, z_m, r_s)$, an analytical expression for FWHM in terms of b, z_m, and r_s is ultimately obtained, which can be expressed as

$$\text{FWHM} = 0.955 \cdot f_2(b, z_m, r_s) - 0.029. \tag{26}$$

Fig. 11(a) and (b) shows the variations of Bias and FWHM with z_m under different r_s when $b = 0.23$ m^{-1}. It can be observed that with fixed b and r_s, a deeper z_m leads to greater Bias and broader FWHM. Fig. 11(c) and (d) shows the variations of Bias and FWHM with z_m under different z_m when $r_s = 27.1$ m. It is evident that with fixed z_m and r_s, a higher b results in greater Bias and broader FWHM. These findings are consistent with the results from the ICESat-2 platform. Fig. 11(e) and (f) shows the variations of Bias and FWHM with r_s under different z_m when $b = 0.23$ m^{-1}. Within a certain range of small r_s, both Bias and FWHM increase with increasing r_s. For the same seawater, as the telescope's FOV increases, the maximum scattering angle of the received photons and the number of multiple scattering events also increase, leading to larger Bias and FWHM. However, once the FOV continues to increase, the telescope can effectively capture photons with various multiple scattering scenarios, resulting in a relatively stable Bias and FWHM. As shown in Fig. 11(f), when the FOV exceeds a certain value (i.e., when r_s exceeds 20 m), the signal broadening is significant, leading to larger uncertainties in locating the peak value of a waveform. Consequently, the peak Bias values in Fig. 11(e) show greater fluctuations though they remain close to a stable value.

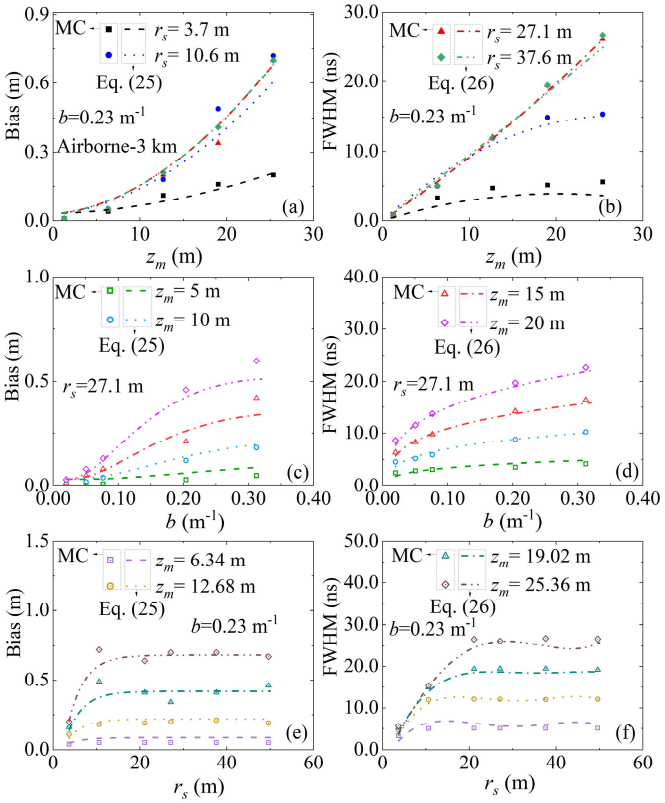

Fig. 11. When $b = 0.23$ m^{-1}, under different r_s conditions. (a) Bias versus z_m and (b) FWHM versus z_m. When $r_s = 27.1$ m, under different z_m conditions. (c) Bias versus b and (d) FWHM versus b. When $b = 0.23$ m^{-1}, under different z_m conditions. (e) Bias versus r_s and (f) FWHM versus r_s. Symbols represent MC simulation results, while lines represent the results calculated using (25) and (26).

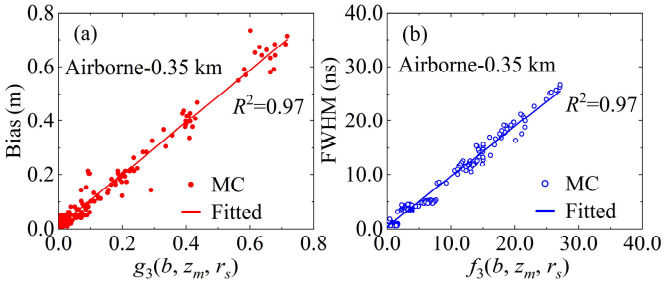

Fig. 12. For Chl ranging from 0.01 to 1.00 mg/m^3, b varies from 0.02 to 0.31 m^{-1}, and z_m ranges from (0.1∼2)/K_d on the Airborne-0.35-km platform. (a) Bias versus $g_3(b, z_m, r_s)$ and (b) FWHM versus $f_3(b, z_m, r_s)$. Symbols represent the MC simulation results, while lines represent the fit results.

C. Airborne-0.35 km

When the flight altitude of the airborne platform is lower, and the variation in the lidar's FOV is minimal, the lidar's r_s is smaller. For example, among the two airborne lidars listed in Table I, the lidar at an altitude of 3 km has an r_s of 37.6 m, whereas the lidar at a height of 0.35 km has an r_s of only 1.15 m. Therefore, for the airborne lidar at 0.35 km, a quantitative analysis is conducted on the effects of b, z_m, and r_s on the peak Bias and FWHM of the seabed backscattered signal, using the statistical methods described above. The results are shown in Fig. 12. The expressions for

TABLE II
VALUE OF FIT COEFFICIENT

	i=0	i=1	i=2	i=3	i=4
m_i	-0.07	0.19	$9.30\cdot10^{-3}$	$1.61\cdot10^{-4}$	-
n_i	-0.47	0.32	-0.04	$1.00\cdot10^{-4}$	-
p_i	-0.29	0.27	-0.01	$1.94\cdot10^{-4}$	-
q_i	0.01	-0.01	$8.08\cdot10^{-4}$	$-1.80\cdot10^{-5}$	-
r_i	-0.72	2.68	-1.19	0.21	$-1.25\cdot10^{-2}$
t_i	0.42	-2.70	1.60	-0.32	0.02
w_i	-0.26	0.76	-0.10	$2.47\cdot10^{-3}$	-
v_i	0.01	-0.03	0.009	$-8\cdot10^{-4}$	-

the normalized variables $g_3(b, z_m, r_s)$ and $f_3(b, z_m, r_s)$ are

$$g_3(b, z_m, r_s) = \sum_{i=0}^{4} \left(m_i \cdot r_s^i\right) \cdot h_2(b, z_m) + \sum_{i=0}^{4} \left(n_i \cdot r_s^i\right) \cdot [h_2(b, z_m)]^2 \quad (27)$$

$$f_3(b, z_m, r_s) = \sum_{i=0}^{4} \left(p_i \cdot r_s^i\right) \cdot j_2(b, z_m) + \sum_{i=0}^{4} \left(q_i \cdot r_s^i\right) \cdot \left[j_2(b, z_m)\right]^2 \quad (28)$$

where m_i, n_i, p_i, and q_i are the coefficients obtained from fitting, with specific values listed in Table II. The normalized variables $h_2(b, z_m)$ and $j_2(b, z_m)$ are the functions of b and z_m, and are expressed as follows:

$$h_2(b, z_m) = \left[0.03 - 0.16 \cdot b + 0.57 \cdot b^2\right] \cdot (b \cdot z_m) + [-0.02 - 0.02 \cdot \ln(b - 0.02)] \cdot (b \cdot z_m)^2 \quad (29)$$

$$j_2(b, z_m) = \left[e^{0.49} \Big/ \left(b + 9.29 \cdot 10^{-3}\right)^{0.70}\right] \cdot (b \cdot z_m). \quad (30)$$

The final expressions for Bias as a function of b, z_m, and r_s, as well as for FWHM as a function of b, z_m, and r_s, are presented as follows:

$$\text{Bias} = 0.009 + 0.964 \cdot g_3(b, z_m, r_s) \quad (31)$$

$$\text{FWHM} = 0.426 + 0.928 \cdot f_3(b, z_m, r_s). \quad (32)$$

D. Shipborne

Similarly, for the shipborne lidar, a quantitative analysis is conducted on the effects of b, z_m, and r_s on the peak Bias and FWHM of the seabed reflected signal, using the statistical methods described above. The results are shown in Fig. 13. The expressions for the normalized variables $g_4(b, z_m, r_s)$ and $f_4(b, z_m, r_s)$ are presented as follows:

$$g_4(b, z_m, r_s) = \sum_{i=0}^{4} \left(r_i \cdot r_s^i\right) \cdot h_3(b, z_m) + \sum_{i=0}^{4} \left(t_i \cdot r_s^i\right) \cdot [h_3(b, z_m)]^2 \quad (33)$$

$$f_4(b, z_m, r_s) = \sum_{i=0}^{3} \left(w_i \cdot r_s^i\right) \cdot j_3(b, z_m) + \sum_{i=0}^{3} \left(v_i \cdot r_s^i\right) \cdot \left[j_3(b, z_m)\right]^2 \quad (34)$$

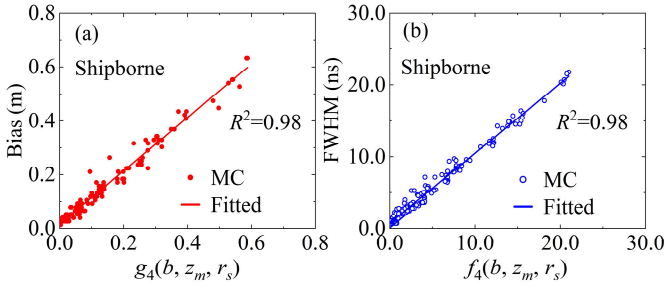

Fig. 13. For Chl ranging from 0.01 to 1.00 mg/m^3, b varies from 0.02 to 0.31 m^{-1}, and z_m ranges from $(0.1\sim2)/K_d$ on the shipborne platform. (a) Bias versus $g_4(b, z_m, r_s)$ and (b) FWHM versus $f_4(b, z_m, r_s)$. Symbols represent the MC simulation results, while lines represent the fit results.

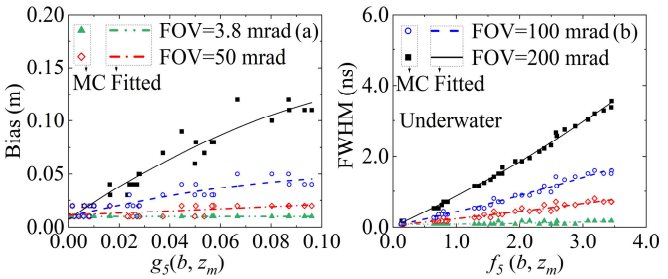

Fig. 14. For Chl ranging from 0.01 to 1.00 mg/m^3, correspondingly, b ranging from 0.02 to 0.31 m^{-1}, and z_m within the range of $(0.1\sim2)/K_d$ on the underwater platform. (a) Bias versus $g_5(b, z_m)$ and (b) FWHM versus $f_5(b, z_m)$. Symbols represent the MC simulation results, while lines represent the fit results.

where r_i, t_i, w_i, and v_i are the coefficients obtained from fitting, with specific values listed in Table II. The normalized variables $h_3(b, z_m)$ and $j_3(b, z_m)$ are the functions of b and z_m, and are expressed as follows:

$$h_3(b, z_m) = \left[2.41 \cdot 10^{-3} + 7.28 \cdot 10^{-3} \ln(b - 0.02)\right] \cdot (b \cdot z_m) + \left[-3.19 \cdot 10^{-3} + 1.20 \cdot 10^{-2} \ln(b - 0.02)\right] \cdot (b \cdot z_m)^2 \quad (35)$$

$$j_3(b, z_m) = \left[e^{0.47}/(b + 0.02)^{0.43}\right] \cdot (b \cdot z_m) + \left[e^{-4.52}/(b + 0.05)^{1.88}\right] \cdot (b \cdot z_m)^2. \quad (36)$$

The final expressions for Bias as a function of b, z_m, and r_s, as well as for FWHM as a function of b, z_m, and r_s, are presented as follows:

$$\text{Bias} = 0.016 + 0.990 \cdot g_4(b, z_m, r_s) \quad (37)$$

$$\text{FWHM} = 0.741 + 0.974 \cdot f_4(b, z_m, r_s). \quad (38)$$

E. Underwater

Deploying lidar underwater not only avoids interference from the air–sea interface, but also enables its integration onto underwater platforms, such as AUVs and ROVs, thereby facilitating deep-sea ocean environment profiling. Consequently, underwater lidar has recently been proposed and demonstrated [67], [68], [69], [70]. Similarly, using the parameters of the underwater lidar from Table I, a quantitative analysis is conducted on the effects of b, z_m, and r_s on the peak Bias and FWHM of the seabed reflected signal, using the statistical methods described above. The results are shown in Fig. 14.

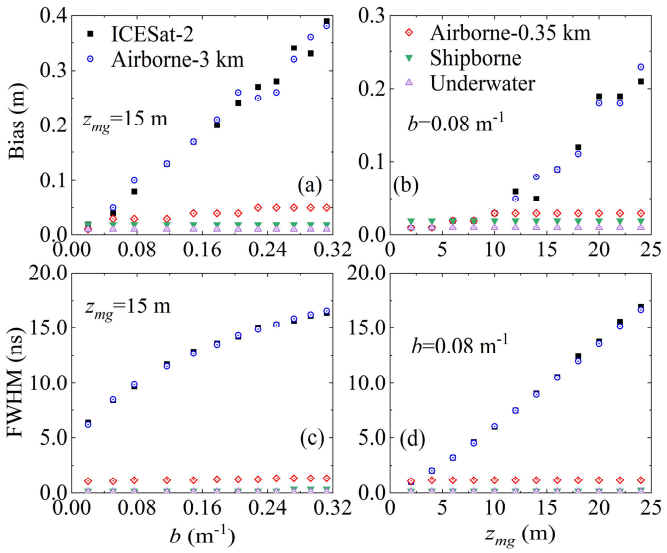

Fig. 15. (a) Bias versus b when $z_{mg} = 15$ m. (b) Bias versus z_{mg} when $b = 0.08$ m^{-1}. (c) FWHM versus b when $z_{mg} = 15$ m. (d) FWHM versus z_{mg} when $b = 0.08$ m^{-1}, for four different platforms.

The expressions for the normalized variables $g_5(b, z_m)$ and $f_5(b, z_m)$ are presented as follows:

$$g_5(b, z_m) = \left[-4.15 \cdot 10^{-4} - 3.10 \cdot 10^{-4} \ln(b - 0.02)\right] \times (b \cdot z_m)^{[1.38-0.22 \cdot \ln(b-0.021)]} \quad (39)$$

$$f_5(b, z_m) = \left[e^{-1.94} \Big/ \left(b + 9.76 \cdot 10^{-4}\right)^{0.85}\right] \cdot (b \cdot z_m). \quad (40)$$

The differences in Bias and FWHM for different platforms under the same b and z_{mg} conditions are shown in Fig. 15. Fig. 15(a) and (c) displays the variation in Bias and FWHM with b when $z_{mg} = 15$ m, while Fig. 15(b) and (d) illustrates the variation in Bias and FWHM with z_{mg} when $b = 0.08$ m^{-1}. It is evident that both Bias and FWHM increase with higher platform height and larger r_s. Specifically, the results for Airborne-3 km are similar to those for ICESat-2, as both platforms have r_s values greater than 20 m. Although the r_s for the Airborne-3 km is larger than that of ICESat-2, it is sufficiently large at this height, so the results are not significantly affected by changes in the r_s. Similarly, shipborne and underwater lidars have smaller r_s, resulting in smaller Bias and FWHM. Additionally, the r_s of the Airborne-0.35-km lidar falls between those of the other two types of platforms, leading to Bias and FWHM values that are also intermediate. In summary, both Bias and FWHM are influenced by r_s, b, and z_m. When these parameters are large, the correction model proposed above should be used to correct the depth data obtained from bathymetric lidar measurements.

F. Impact of Scattering Phase Function

The scattering phase function determines the distribution of the light field underwater [71], which, in turn, affect the distribution of Bias and FWHM of seabed backscattered signal. To investigate the influence of different scattering phase functions on the distribution of Bias and FWHM, this work

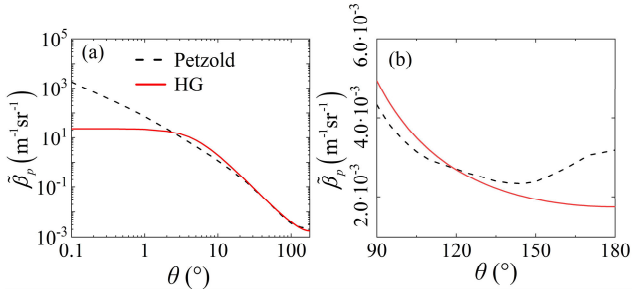

Fig. 16. Comparison of the Petzold scattering phase function and the HG scattering phase function for angles (a) 0°–180° and (b) 90°–180°. Dashed lines represent Petzold, while solid lines represent HG.

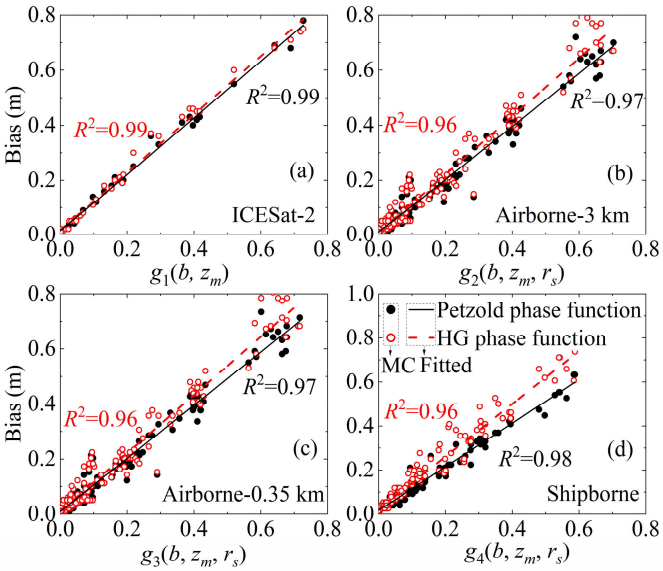

Fig. 17. Comparison of Bias under four platforms for Chl ranging from 0.01 to 1.00 mg/m^3, correspondingly, b ranging from 0.02 to 0.31 m^{-1}, and z_m within the range of $(0.1\sim2)/K_d$ between HG and Petzold scattering phase functions. (a) ICESat-2. (b) Airborne-3 km. (c) Airborne-0.35 km. (d) Shipborne. Symbols represent the MC simulation results, while lines represent the fit results.

incorporates the Henyey–Greenstein (HG) scattering phase function, which significantly differs from the previously used Petzold scattering phase function, for conducting the MC study. The HG function can be expressed as [72]

$$\tilde{\beta}_p = \frac{1}{4\pi} \frac{1 - g^2}{\left[1 + g^2 - 2g\cos(\theta)\right]^{3/2}} \quad (41)$$

where g is the anisotropy parameter, which is set to 0.919 in the simulation [44].

Fig. 16 shows the comparison of the Petzold and HG scattering phase functions. The Petzold function is stronger than the HG function at angles below 5° and between 135° and 180°, as shown in Fig. 16(b). Additionally, the Petzold function increases monotonically in the 135°–180° range, while the HG function decreases monotonically.

After replacing the Petzold scattering phase function with the HG scattering phase function, the MC simulations are rerun, and the relationships of Bias and FWHM with b, z_m, and r_s are recalculated. The differences in Bias and FWHM under these two scattering phase functions are compared,

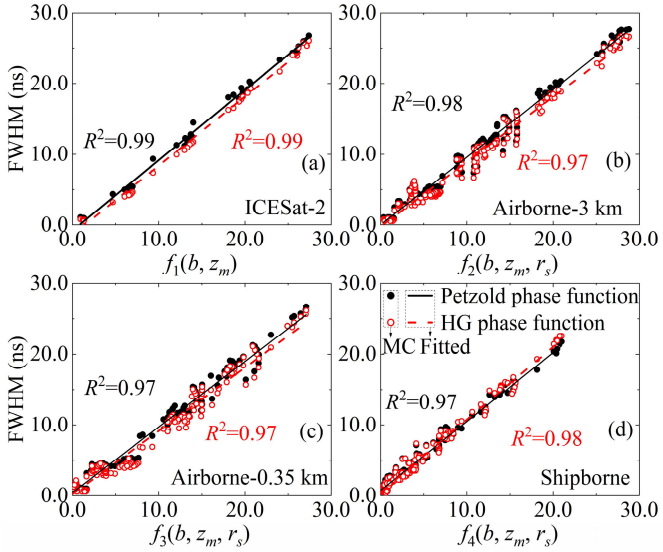

Fig. 18. Comparison of FWHM under four platforms for Chl ranging from 0.01 to 1.00 mg/m^3, correspondingly, b ranging from 0.02 to 0.31 m^{-1}, and z_m within the range of $(0.1\sim2)/K_d$ between HG and Petzold scattering phase functions. (a) ICESat-2. (b) Airborne-3 km. (c) Airborne-0.35 km. (d) Shipborne. Symbols represent the MC simulation results, while lines represent the fit results.

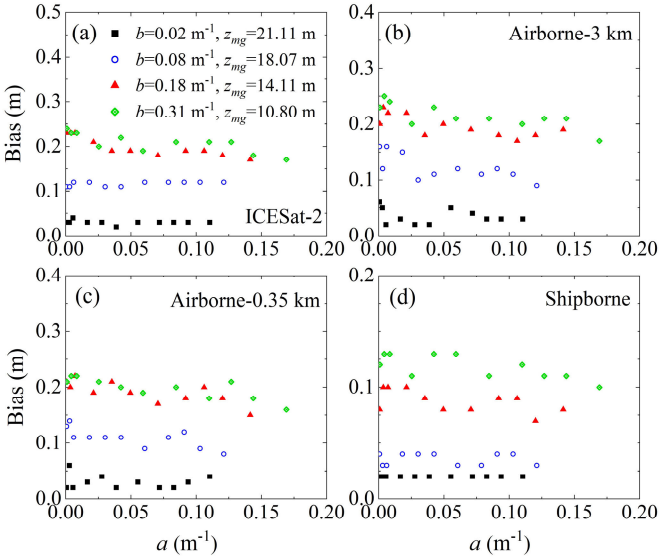

Fig. 19. Effect of a on Bias under different values of b and z_{mg} for different platforms. (a) ICESat-2. (b) Airborne-3 km. (c) Airborne-0.35 km. (d) Shipborne.

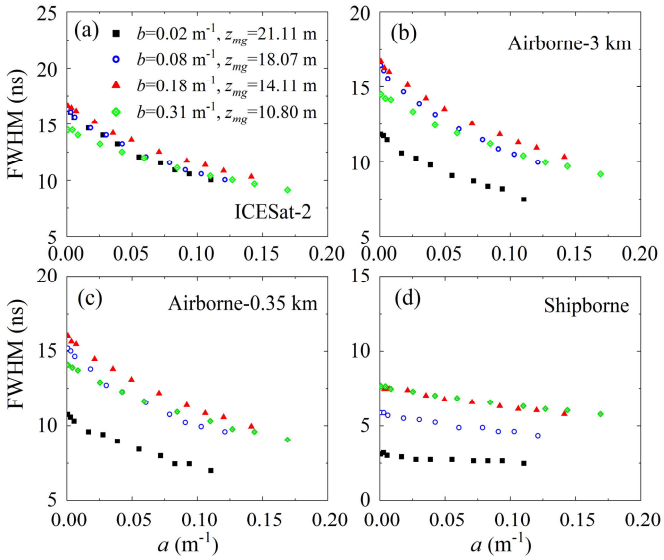

Fig. 20. Effect of a on FWHM under different values of b and z_{mg} for different platforms. (a) ICESat-2. (b) Airborne-3 km. (c) Airborne-0.35 km. (d) Shipborne.

with the results shown in Figs. 17 and 18, respectively. As shown in Figs. 17 and 18, the differences in Bias and FWHM calculated using these two scattering phase functions are minimal. As shown in Fig. 17, for Bias, the results from both scattering phase functions are almost identical for the ICESat-2; however, for the Airborne-3-km platforms, Airborne-0.35-km platforms, and Shipborne platforms, the results from the HG scattering phase function are slightly larger than those from Petzold. As shown in Fig. 18, for FWHM, the results from both scattering phase functions are almost identical to those from the Shipborne platform, whereas for the other three platforms, the results from the HG scattering phase function are slightly smaller than those from Petzold.

G. Impact of the Absorption Coefficient

The variation in a leads to changes in both c and the single scattering albedo (b/c). Therefore, it is important to further investigate the influence of a on Bias and FWHM.

As shown in Fig. 19, for different platforms, when b and z_{mg} are fixed, the variation in a has little impact on bias. This is because an increase in a leads to an increase in c, which, in turn, reduces the photon step length (s), causing more scattering events when photons reach the same depth. However, as c increases, b/c decreases, meaning that the increase in c accelerates energy attenuation, which reduces the probability of multiple scattering events. The interaction between the shortened step length and the accelerated energy attenuation largely counteracts each other, ultimately making the effect of a on Bias negligible.

However, as shown in Fig. 20, an increase in a leads to a gradual reduction in FWHM. This is because, when b and z_{mg} remain constant, a higher a reduces the single scattering albedo, thereby accelerating photon energy attenuation. Consequently, when photons travel the same distance in water, a higher a results in faster energy loss of photons, leading to a reduction in FWHM. Therefore, when analyzing the influence of multiple scattering on bottom reflection width based on the FWHM statistical model, the contribution of a must be considered.

IV. Conclusion

Bathymetric lidar has widespread applications. However, due to the significant forward scattering of the laser beam as it transmits through water, there is a notable contribution of multiple scattering in the seabed reflected signals. This leads to a shift in the peak position of the seabed reflected signal

(termed Bias) and broadening of the signal width (termed FWHM). To quantitatively study the impact of multiple scattering on Bias and FWHM, this study employs semianalytic MC simulations to statistically analyze the models for Bias and FWHM of bathymetric lidar across different platforms, including spaceborne, airborne, shipborne, and underwater platforms.

The results indicate that b, z_m, and r_s collectively influence Bias and FWHM. As b, z_m, and r_s increase, Bias and FWHM increase. This means that b, z_m, and r_s together affect the proportion of multiple scatterings in the reflected signals. The higher the proportion of multiple scattering signals, the greater the deviation of the peak determined from the reflected waveform, and the more broadening of the signal width. This not only leads to an overestimation of bottom depth when the peak position of the seabed signal is used for evaluation, but also makes extracting the peak position (i.e., determining the bottom depth) more challenging due to the broadening of the seabed signal. Specifically, for bathymetric lidar systems operating at higher altitudes, including Airborne-3 km, Airborne-0.35 km, and spaceborne lidar, the Bias can reach up to nearly 0.8 m, and the FWHM can be as high as 30 ns when b is below 0.31 m^{-1} and z_m is less than $2/K_d$. For shipborne bathymetric lidar systems, the Bias and FWHM are lower, with maximum values of approximately 0.6 m and 20 ns, respectively. For underwater lidar, due to the unique characteristics of underwater operations, the bottom-reflected signal is least affected by multiple scattering, resulting in the smallest Bias and FWHM. These findings suggest that for bathymetric lidar with larger r_s, depth measurements in waters under higher multiple scattering and deeper bottom depths may be overestimated and thus require correction. Moreover, statistical analysis shows that Bias is minimally affected by the absorption coefficient, while FWHM decreases with increasing absorption coefficient. Finally, the empirical expressions derived from the statistical analysis for Bias and FWHM concerning b, z_m, and r_s provide valuable guidance for correcting depth measurement errors caused by multiple scattering in bathymetric lidar.

Based on the above, we will further investigate the mechanism regarding the impact of multiple scattering on Bias and FWHM, with an aim of developing a generic expression for bias and FWHM applicable to different platforms, rather than using separate expressions for each platform as presented in this study. Moreover, the interference of the air–sea interface will also be further investigated, and the applicability of the derived empirical expressions will be experimentally verified. Additionally, while this work focuses on the 532-nm wavelength, future studies will consider additional wavelengths to enhance the robustness of the model. In conclusion, the empirical models developed in this study offer important insights for enhancing the accuracy of bottom depth detection across various platforms.

REFERENCES

[1] M. Milli, "Nautical cartography as a tool of international maritime cooperation: Some Italian cases in the Mediterranean Sea," *Ocean Coastal Manage.*, vol. 213, Nov. 2021, Art. no. 105876.

[2] A. Šiljeg et al., "GIS modelling of bathymetric data in the construction of port terminals—An example of Vlaška channel in the Port of Ploče, Croatia," *Int. J. Eng. Model.*, vol. 32, no. 1, pp. 17–37, Aug. 2019.

[3] G. Inglis, C. Smart, I. Vaughn, and C. Roman, "A pipeline for structured light bathymetric mapping," in *Proc. IEEE/RSJ Int. Conf. Intell. Robots Syst.*, Oct. 2012, pp. 4425–4432.

[4] S.-W. Huang, E. Chen, and J. Guo, "Efficient seafloor classification and submarine cable route design using an autonomous underwater vehicle," *IEEE J. Ocean. Eng.*, vol. 43, no. 1, pp. 7–18, Jan. 2018.

[5] M. Ashphaq, P. K. Srivastava, and D. Mitra, "Review of near-shore satellite derived bathymetry: Classification and account of five decades of coastal bathymetry research," *J. Ocean Eng. Sci.*, vol. 6, no. 4, pp. 340–359, Dec. 2021.

[6] N. Mukherjee et al., "From bathymetry to bioshields: A review of post-tsunami ecological research in India and its implications for policy," *Environ. Manage.*, vol. 46, no. 3, pp. 329–339, Sep. 2010.

[7] M. M. Wieczorek, W. A. Spallek, T. Niedzielski, J. A. Godbold, and I. G. Priede, "Use of remotely-derived bathymetry for modelling biomass in marine environments," *Pure Appl. Geophys.*, vol. 171, no. 6, pp. 1029–1045, Jun. 2014.

[8] F. Bandini et al., "Bathymetry observations of inland water bodies using a tethered sing-beam sonar controlled by an unmanned aerial vehicle," *Hydrol. Earth Syst. Sci.ss*, vol. 25, pp. 4549–4565, Jul. 2008.

[9] Z. Li et al., "Exploring modern bathymetry: A comprehensive review of data acquisition devices, model accuracy, and interpolation techniques for enhanced underwater mapping," *Frontiers Mar. Sci.*, vol. 10, May 2023, Art. no. 1178845.

[10] E. Bok, J. J. Park, H. Choi, C. K. Han, O. B. Wright, and S. H. Lee, "Metasurface for water-to-air sound transmission," *Phys. Rev. Lett.*, vol. 120, no. 4, Jan. 2018, Art. no. 044302.

[11] M. Miron-Morin, D. R. Barclay, and J.-F. Bousquet, "The oceanographic sensitivity of the acoustic channel in shallow water," *IEEE J. Ocean. Eng.*, vol. 46, no. 2, pp. 675–686, Apr. 2021.

[12] J. Wei et al., "Shallow water bathymetry with multi-spectral satellite ocean color sensors: Leveraging temporal variation in image data," *Remote Sens. Environ.*, vol. 250, Dec. 2020, Art. no. 112035.

[13] D. R. Lyzenga, "Remote sensing of bottom reflectance and water attenuation parameters in shallow water using aircraft and Landsat data," *Int. J. Remote Sens.*, vol. 2, no. 1, pp. 71–82, Jan. 1981.

[14] D. R. Lyzenga, "Passive remote sensing techniques for mapping water depth and bottom features," *Appl. Opt.*, vol. 17, no. 3, pp. 379–383, 1978.

[15] Z. Lee, K. L. Carder, C. D. Mobley, R. G. Steward, and J. S. Patch, "Hyperspectral remote sensing for shallow waters: 2. Deriving bottom depths and water properties by optimization," *Appl. Opt.*, vol. 38, no. 18, pp. 3831–3843, Jun. 1999.

[16] W. Lai, Z. Lee, J. Wang, Y. Wang, R. Garcia, and H. Zhang, "A portable algorithm to retrieve bottom depth of optically shallow waters from top-of-atmosphere measurements," *J. Remote Sens.*, vol. 2022, 2022, Art. no. 9831947.

[17] B. Collister et al., "Assessing the utility of high spectral resolution LiDAR for measuring particulate backscatter in the ocean and evaluating satellite ocean color retrievals," *Remote Sens. Environ.*, vol. 300, Jan. 2024, Art. no. 113898.

[18] I. Joint and S. B. Groom, "Estimation of phytoplankton production from space: Current status and future potential of satellite remote sensing," *J. Exp. Mar. Biol. Ecol.*, vol. 250, nos. 1–2, pp. 233–255, Jul. 2000.

[19] G. Mandlburger and B. Jutzi, "On the feasibility of water surface mapping with single photon LiDAR," *ISPRS Int. J. Geo-Inf.*, vol. 8, no. 4, p. 188, Apr. 2019.

[20] M. Shangguan et al., "Sensing profiles of the volume scattering function at 180° using a single-photon oceanic fluorescence LiDAR," *Opt. Exp.*, vol. 31, no. 24, pp. 40393–40410, 2023.

[21] K. Guo et al., "Development of a single-wavelength airborne bathymetric LiDAR: System design and data processing," *ISPRS J. Photogramm. Remote Sens.*, vol. 185, pp. 62–84, Mar. 2022.

[22] P. J. Kinzel, C. J. Legleiter, and J. M. Nelson, "Mapping river bathymetry with a small footprint green LiDAR: Applications and challenges[1]," *JAWRA J. Amer. Water Resources Assoc.*, vol. 49, no. 1, pp. 183–204, Feb. 2013.

[23] S. E. Mitchell and J. P. Thayer, "Ranging through shallow semitransparent media with polarization LiDAR," *J. Atmos. Ocean. Technol.*, vol. 31, no. 3, pp. 681–697, Mar. 2014.

[24] D. Ventura, "Coastal zone mapping with the world's first airborne multibeam bathymetric LiDAR mapping system," *Hydrogr. Nachrichten*, vol. 115, pp. 48–53, Jul. 2020.

[25] C. E. Parrish, L. A. Magruder, A. L. Neuenschwander, N. Forfinski-Sarkozi, M. Alonzo, and M. Jasinski, "Validation of ICESat-2 ATLAS bathymetry and analysis of ATLAS's bathymetric mapping performance," *Remote Sens.*, vol. 11, no. 14, p. 1634, Jul. 2019.

[26] L. A. Magruder, J. Markel, and C. Simurda, "An overview of ICESat-2 bathymetric capabilities and discoveries," *Proc. SPIE*, vol. 12110, pp. 69–80, Jun. 2022.

[27] M. Shangguan, Z. Yang, Z. Lin, Z. Lee, H. Xia, and Z. Weng, "Compact long-range single-photon underwater LiDAR with high spatial–temporal resolution," *IEEE Geosci. Remote Sens. Lett.*, vol. 20, pp. 1–5, 2023.

[28] K. Guo et al., "Errors of airborne bathymetry LiDAR detection caused by ocean waves and dimension-based laser incidence correction," *Remote Sens.*, vol. 13, no. 9, p. 1750, Apr. 2021.

[29] Y. Ma et al., "Satellite-derived bathymetry using the ICESat-2 LiDAR and Sentinel-2 imagery datasets," *Remote Sens. Environ.*, vol. 250, Dec. 2020, Art. no. 112047.

[30] C. Liu et al., "Accurate refraction correction—Assisted bathymetric inversion using ICESat-2 and multispectral data," *Remote Sens.*, vol. 13, no. 21, p. 4355, Oct. 2021.

[31] H. Aasen, E. Honkavaara, A. Lucieer, and P. Zarco-Tejada, "Quantitative remote sensing at ultra-high resolution with UAV spectroscopy: A review of sensor technology, measurement procedures, and data correction workflows," *Remote Sens.*, vol. 10, no. 7, p. 1091, 2018.

[32] Y. Chen, Z. Zhu, Y. Le, Z. Qiu, C. Gang, and L. Wang, "Refraction correction and coordinate displacement compensation in nearshore bathymetry using ICESat-2 LiDAR data and remote-sensing images," *Opt. Exp.*, vol. 29, no. 2, pp. 2411–2430, 2021.

[33] W. Xu et al., "Refraction error correction of airborne LiDAR bathymetry data considering sea surface waves," *Int. J. Appl. Earth Observ. Geoinf.*, vol. 102, Oct. 2021, Art. no. 102402.

[34] F. Yang, D. Su, Y. Ma, C. Feng, A. Yang, and M. Wang, "Refraction correction of airborne LiDAR bathymetry based on sea surface profile and ray tracing," *IEEE Trans. Geosci. Remote Sens.*, vol. 55, no. 11, pp. 6141–6149, Nov. 2017.

[35] F. Yang et al., "Modeling and analyzing water column forward scattering effect on airborne LiDAR bathymetry," *IEEE J. Ocean. Eng.*, vol. 48, no. 4, pp. 1373–1388, Oct. 2023.

[36] J. Yang, Y. Ma, H. Zheng, Y. Gu, H. Zhou, and S. Li, "Analysis and correction of water forward-scattering-induced bathymetric bias for spaceborne photon-counting LiDAR," *Remote Sens.*, vol. 15, no. 4, p. 931, Feb. 2023.

[37] G. C. Guenther, A. Cunningham, P. E. LaRocque, and D. Reid, "Meeting the accuracy challenge in airborne LiDAR bathymetry," in *Proc. EARSeL-SIG-Workshop LiDAR*, Jan. 2000, pp. 1–27.

[38] C. Wang, Q. Li, Y. Liu, G. Wu, P. Liu, and X. Ding, "A comparison of waveform processing algorithms for single-wavelength LiDAR bathymetry," *ISPRS J. Photogramm. Remote Sens.*, vol. 101, pp. 22–35, Mar. 2015.

[39] G. C. Guenther and R. W. Thomas, "Effects of propagation-induced pulse stretching in airborne laser hydrography," *Proc. SPIE*, vol. 489, pp. 287–296, Sep. 1984.

[40] D. J. Spence, B. R. Neimann, and H. M. Pask, "Monte Carlo modelling for elastic and Raman signals in oceanic LiDAR," *Opt. Exp.*, vol. 31, no. 8, pp. 12339–12348, 2023.

[41] Q. Liu et al., "A semianalytic Monte Carlo radiative transfer model for polarized oceanic LiDAR: Experiment-based comparisons and multiple scattering effects analyses," *J. Quant. Spectrosc. Radiat. Transf.*, vol. 237, Nov. 2019, Art. no. 106638.

[42] D. Liu et al., "LiDAR remote sensing of seawater optical properties: Experiment and Monte Carlo simulation," *IEEE Trans. Geosci. Remote Sens.*, vol. 57, no. 11, pp. 9489–9498, Nov. 2019.

[43] Y. Liao, M. Shangguan, Z. Yang, Z. Lin, Y. Wang, and S. Li, "GPU-accelerated Monte Carlo simulation for a single-photon underwater LiDAR," *Remote Sens.*, vol. 15, no. 21, p. 5245, Nov. 2023.

[44] P. Chen, C. Jamet, Z. Mao, and D. Pan, "OLE: A novel oceanic LiDAR emulator," *IEEE Trans. Geosci. Remote Sens.*, vol. 59, no. 11, pp. 9730–9744, Nov. 2021.

[45] P. Chen, D. Pan, Z. Mao, and H. Liu, "Semi-analytic Monte Carlo model for oceanographic LiDAR systems: Lookup table method used for randomly choosing scattering angles," *Appl. Sci.*, vol. 9, no. 1, p. 48, Dec. 2018.

[46] Q. Liu et al., "A semianalytic Monte Carlo simulator for spaceborne oceanic LiDAR: Framework and preliminary results," *Remote Sens.*, vol. 12, no. 17, p. 2820, Aug. 2020.

[47] H. He et al., "Validation of the polarized Monte Carlo model of shipborne oceanic LiDAR returns," *Opt. Exp.*, vol. 31, no. 26, pp. 43250–43268, 2023.

[48] D. Wu, P. Chen, W. Kong, and D. Pan, "A novel semi-analytical method for modeling polarized oceanic profiling LiDAR multiple scattering signals," *IEEE Trans. Geosci. Remote Sens.*, vol. 62, 2024, Art. no. 3369099.

[49] L. R. Poole, D. D. Venable, and J. W. Campell, "Semianalytic Monte Carlo radiative transfer model for oceanographic LiDAR systems," *Appl. Opt.*, vol. 20, no. 20, pp. 3653–3656, 1981.

[50] C. Li, G. Zhou, and D. Zhang, "Analysis of affecting factors for laser underwater transmission echo signals based on semi-analytic Monte Carlo," *Int. J. Remote Sens.*, vol. 45, nos. 19–20, pp. 7185–7211, Oct. 2024.

[51] J. Li et al., "Range difference between shallow and deep channels of airborne bathymetry LiDAR with segmented field-of-view receivers," *IEEE Trans. Geosci. Remote Sens.*, vol. 60, 2022, Art. no. 3172351.

[52] C. D. Mobley, H. Zhang, and K. J. Voss, "Effects of optically shallow bottoms on upwelling radiances: Bidirectional reflectance distribution function effects," *Limnol. Oceanogr.*, vol. 48, no. 1, pp. 337–345, 2003.

[53] A. Morel and S. Maritorena, "Bio-optical properties of oceanic waters: A reappraisal," *J. Geophys. Res., Oceans*, vol. 106, no. C4, pp. 7163–7180, Apr. 2001.

[54] Z. Lee, J. Wei, K. Voss, M. Lewis, A. Bricaud, and Y. Huot, "Hyperspectral absorption coefficient of 'pure' seawater in the range of 350–550 nm inverted from remote sensing reflectance," *Appl. Opt.*, vol. 54, no. 3, pp. 546–558, 2015.

[55] L. Prieur and S. Sathyendranath, "An optical classification of coastal and oceanic waters based on the specific spectral absorption curves of phytoplankton pigments, dissolved organic matter, and other particulate materials[1]," *Limnology Oceanogr.*, vol. 26, no. 4, pp. 671–689, Jul. 1981.

[56] A. Morel, "Optical properties of pure water and pure sea water," *Opt. Aspects Oceanogr.*, vol. 1, no. 1, pp. 1–24, 1974.

[57] X. Zhang and L. Hu, "Scattering by pure seawater at high salinity," *Opt. Exp.*, vol. 17, no. 15, pp. 12685–12691, 2009.

[58] A. Morel, "Optical modeling of the upper ocean in relation to its biogenous matter content (case I waters)," *J. Geophys. Res.*, vol. 93, no. C9, pp. 10749–10768, 1988.

[59] Z. P. Lee, K. P. Du, and R. Arnone, "A model for the diffuse attenuation coefficient of downwelling irradiance," *J. Geophys. Res.*, vol. 110, no. C2, pp. C02016.1–C02016.10, 2005.

[60] T. J. Petzold, "Volume scattering functions for selected ocean waters," Scripps Inst. Oceanogr., San Diego, CA, USA, 1972.

[61] T. A. Neumann et al., "The ice, cloud, and land elevation satellite—2 mission: A global geolocated photon product derived from the advanced topographic laser altimeter system," *Remote Sens. Environ.*, vol. 233, Nov. 2019, Art. no. 111325.

[62] P. Chen et al., "Vertical distribution of subsurface phytoplankton layer in South China sea using airborne LiDAR," *Remote Sens. Environ.*, vol. 263, Sep. 2021, Art. no. 112567.

[63] H. Liu, P. Chen, Z. Mao, D. Pan, and Y. He, "Subsurface plankton layers observed from airborne LiDAR in Sanya Bay, South China Sea," *Opt. Exp.*, vol. 26, no. 22, pp. 29134–29147, 2018.

[64] P. Chen and D. Pan, "Ocean optical profiling in South China sea using airborne LiDAR," *Remote Sens.*, vol. 11, no. 15, p. 1826, Aug. 2019.

[65] P. Xu et al., "Design and validation of a shipborne multiple-field-of-view LiDAR for upper ocean remote sensing," *J. Quant. Spectrosc. Radiat. Transf.*, vol. 254, Oct. 2020, Art. no. 107201.

[66] Z. Lee, L. Zhao, C. Hu, D. Wang, J. Lin, and S. Shang, "Absorption coefficient and chlorophyll concentration of oceanic waters estimated from band difference of satellite-measured remote sensing reflectance," *J. Remote Sens.*, vol. 3, p. 63, Jan. 2023.

[67] M. Shangguan, Z. Liao, and Y. Guo, "Simultaneous sensing profiles of beam attenuation coefficient and volume scattering function at 180° using a single-photon underwater elastic-Raman LiDAR," *Opt. Exp.*, vol. 32, no. 5, pp. 8189–8204, Jan. 2024.

[68] M. Shangguan, Z. Yang, Z. Lin, Z. Weng, and J. Sun, "Full-day profiling of a beam attenuation coefficient using a single-photon underwater LiDAR with a large dynamic measurement range," *Opt. Lett.*, vol. 49, no. 3, pp. 626–629, 2024.

[69] M. Shangguan et al., "Day and night continuous high-resolution shallow-water depth detection with single-photon underwater LiDAR," *Opt. Exp.*, vol. 31, no. 26, pp. 43950–43962, 2023.

[70] M. Shangguan et al., "Remote sensing oil in water with an all-fiber underwater single-photon Raman LiDAR," *Appl. Opt.*, vol. 62, no. 19, pp. 5301–5305, 2023.
[71] J. H. Churnside and J. A. Shaw, "LiDAR remote sensing of the aquatic environment," *Appl. Opt.*, vol. 59, no. 10, pp. C92–C99, 2020.
[72] L. C. Henyey and J. L. Greenstein, "Diffuse radiation in the galaxy," *Astrophys. J.*, vol. 93, pp. 70–83, Jan. 1941.

Mingjia Shangguan received the Ph.D. degree from the University of Science and Technology of China, Hefei, China, in 2017.

He is currently an Associate Professor with the State Key Laboratory of Marine Environmental Science, College of Ocean and Earth Sciences, Xiamen University, Xiamen, China. He has authored or co-authored more than 40 peer-reviewed journal articles and holds 50 Chinese national invention patents as well as one U.S. patent. His main research interests focus on single-photon lidar and its applications in marine, atmospheric, and target imaging.

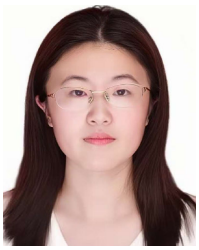

Zhuoyang Liao received the bachelor's degree from Xiamen University, Xiamen, Fujian, China, in June 2024.

Her main research area is the retrieval of optical parameters using underwater single-photon lidar.

Yirui Guo received the bachelor's degree from Xiamen University, Xiamen, Fujian, China, in June 2024.

Her main research area is the retrieval of optical parameters using underwater single-photon lidar.

Zhongping Lee (Senior Member, IEEE) received the Ph.D. degree from the University of South Florida, Tampa, FL, USA, in 1994.

He is currently a Professor with the State Key Laboratory of Marine Environmental Science, College of Ocean and Earth Sciences, Xiamen University, Xiamen, China. He has authored or co-authored more than 180 peer-reviewed journal articles. He led the development of the widely used quasi-analytical algorithm (QAA) and the hyperspectral algorithm (HOPE) for processing both optically deep and shallow waters, along with various applications of satellite ocean color products. His main research interests are in optical oceanography and ocean color remote sensing.

Dr. Lee is a fellow of the Optical Society of America. He is a member of many science teams for ocean color remote sensing.